



UNIVERSITÀ
DEGLI STUDI
FIRENZE

FLORE

Repository istituzionale dell'Università degli Studi di Firenze

Mechanical response and yielding transition of silk-fibroin and silk-fibroin/cellulose nanocrystals composite gels

Questa è la Versione finale referata (Post print/Accepted manuscript) della seguente pubblicazione:

Original Citation:

Mechanical response and yielding transition of silk-fibroin and silk-fibroin/cellulose nanocrystals composite gels / Poggi G.; Chelazzi D.; Laurati M.. - In: COLLOIDS AND SURFACES. A, PHYSICOCHEMICAL AND ENGINEERING ASPECTS. - ISSN 0927-7757. - ELETTRONICO. - 636:(2022), pp. 128121-128129. [10.1016/j.colsurfa.2021.128121]

Availability:

The webpage <https://hdl.handle.net/2158/1256594> of the repository was last updated on 2024-04-29T16:25:15Z

Published version:

DOI: 10.1016/j.colsurfa.2021.128121

Terms of use:

Open Access

La pubblicazione è resa disponibile sotto le norme e i termini della licenza di deposito, secondo quanto stabilito dalla Policy per l'accesso aperto dell'Università degli Studi di Firenze (<https://www.sba.unifi.it/upload/policy-oa-2016-1.pdf>)

Publisher copyright claim:

Conformità alle politiche dell'editore / Compliance to publisher's policies

Questa versione della pubblicazione è conforme a quanto richiesto dalle politiche dell'editore in materia di copyright.

This version of the publication conforms to the publisher's copyright policies.

La data sopra indicata si riferisce all'ultimo aggiornamento della scheda del Repository FloRe - The above-mentioned date refers to the last update of the record in the Institutional Repository FloRe

(Article begins on next page)

Mechanical response and yielding transition of silk-fibroin and silk-fibroin/cellulose nanocrystals composite gels

G. Poggi¹, D. Chelazzi¹, M. Laurati^{1*}

¹*Department of Chemistry "Ugo Schiff" and CSGI, University of Florence, Via della Lastruccia 3, 50019, Sesto Fiorentino, Florence, Italy.*

Abstract

We investigated the mechanical properties of gels formed by silk fibroin and silk fibroin/cellulose nanocrystal mixtures. Viscosity and linear viscoelasticity measurements showed that the addition of cellulose nanocrystals induces a speed-up of the gelation kinetics and leads to moderately stiffer gels. Combining continuous shear tests and large amplitude oscillatory shear (LAOS) measurements we additionally characterized the shear-induced solid-fluid transition. Continuous shear tests indicated a larger yield stress for the silk fibroin/cellulose nanocrystal gel, confirming thus the stiffening effect. They also revealed that the yield strain of the gels becomes smaller at higher shear rates, possibly as a result of shear-induced compaction. The detailed analysis of the full anharmonic response in LAOS measurements additionally evidenced that the fluidization of the gels is a broad and gradual transition, which is characterized by two different yield strains: one corresponding to the onset of solid melting and one to the complete fluidization of the system.

Keywords: Fibroin gel, rheology, cellulose nanocrystal, yielding

1. Introduction

The development of sustainable biomaterials and green composites is at the forefront of the research efforts in materials science [1, 2]. Sustainable, eco-friendly biomaterials find already application in cancer therapy, orthopedic implants, contact lenses, breast implants, among others. Similarly, composite materials based on biopolymers and natural fibers help solving problems related with the disposal and/or recycling of synthetic polymers and fibers, the high energy cost of their fabrication and the limited reserves of petroleum, which is at the basis of their production. Green composites find use as insulating materials, as panelling for the automotive industry, and as housing for electronic components, among others. A fundamental aspect of the performance of these two classes is their mechanical response, which determines their flexibility, toughness, strength and durability [3, 4].

*Corresponding author

Email address: marco.laurati@unifi.it (M. Laurati¹)

13 Silk fibroin is an abundant natural protein produced by silkworms and spiders. For
 14 applications as biomaterial and in composites, fibroin protein fibers have the advantage
 15 of presenting a high mechanical strength [5, 6]. Fibroin solutions, which are initially in
 16 a fluid state, spontaneously undergo gelation following a two-step process [7, 8]: dur-
 17 ing early stage gelation, initial network formation is driven by hydrogen bonding, hy-
 18 drophobic interactions and electrostatic interactions, without changes in the secondary
 19 structure; later, strong interactions occur leading to the formation of an increasingly
 20 larger fraction of β -sheets which lead to mechanically stable hydrogels [9]. The fibroin
 21 concentration and the processing conditions strongly affect the degree of crosslinking
 22 and the bond strength, thus the mechanical response of the gel [8]. A few studies in-
 23 vestigated also the non-linear rheological response of fibroin solutions and gels, show-
 24 ing the presence of strain hardening effects at sufficiently large fibroin concentration
 25 [10, 11, 12, 13, 14]. Additionally, the gelation kinetics, which are typically slow [15],
 26 are particularly sensitive to pH, temperature and ionic strength [7, 16]. The mechanical
 27 properties of fibroin gels can be also tuned through the addition of a second compo-
 28 nent, which can be a synthetic polymer like polyacrylamide [17], polyethylene oxide
 29 [15], polyvinyl alcohol [18] or polyurethane [19], or a natural polymer, like collagen
 30 [20], chitosan [21], pectin [22] or alginate [23], among others. There are also a few
 31 examples of the use of cellulose nanofibers (CNF) and cellulose nanocrystals (CNC)
 32 combined with fibroin to obtain all-natural composite materials [24, 25, 26, 27, 28].
 33 For instance, we recently proposed the use of dispersions of self-regenerated silk fi-
 34 broin (SRSF) extracted from *Bombyx mori* for the consolidation of fragile silk fibers
 35 [29, 30]. To further increase the spectrum of fine adjustment of the mechanical proper-
 36 ties of the dispersions, and thus better meet the needs of silk conservators, SRSF was
 37 blended with CNC.

38 The composition and processing conditions of the composite fibroin gels investigated
 39 in the mentioned studies are typically very diverse and specifically tailored towards
 40 desired applications: it is thus difficult to draw any general conclusion on the effect
 41 of the addition of nanocellulose on the mechanical behavior of these systems. More-
 42 over, mechanical characterization was mainly focused on the measurement of linear
 43 viscoelasticity and viscosity, while the yielding transition of the materials remained
 44 essentially unexplored. Such transition is of primary interest for processing and appli-
 45 cation purposes. To fill this knowledge gap, we compare in this work the mechanical
 46 response of gels formed by pure SRSF dispersions and by SRSF/CNC mixtures with
 47 the same content of SRSF. By combining different rheological techniques and analysis
 48 methods, we determine the viscosity and stiffness of the gels, and we characterize in
 49 great detail the yielding transition. Our findings show that the addition of CNC alters
 50 the gelation kinetics, leads to stronger gels and qualitatively modifies the yielding be-
 51 havior. In addition, by applying the sequence of physical processes (SPP) approach
 52 [31, 32] to the analysis of large amplitude oscillatory strain (LAOS) measurements, we
 53 find evidence of a broad yielding transition for both gels, which is characterized by
 54 a progressive fluidization for which we precisely determine the characteristic strain at
 55 which this process starts and the one at which it is almost complete.

56 2. Materials and Methods

57 2.1. Materials

58 Ethanol (EtOH, analytical grade, Carlo Erba), calcium chloride (dehydrated CaCl_2
59 (powder; > 97.0% (KT), Fluka), and cellulose nanocrystals, commercial white taffetà
60 silk (Casa del tessuto, Florence), CNC (0.7–0.8% of residual sulfur, Celluforce), were
61 used for the preparation of the SRSF and hybrid SRSF-CNC dispersions. Silver nitrate
62 (AgNO_3 , 0.1M, Merck) was used for chloride assays. Ultrapure Milli-Q water (resis-
63 tivity: 18.2 $\text{M}\Omega\cdot\text{cm}$ at 25 °C) was used where needed. The SRSF dispersions were
64 obtained from taffetà silk, using a modified version of the protocol reported elsewhere
65 [30]. The silk textiles were washed with EtOH four times to remove impurities and
66 industrial additives, and let dry at room temperature; then, the textile was immersed
67 in a solution of $\text{CaCl}_2\cdot\text{H}_2\text{O}:\text{EtOH}$ (molar ratio of 1:8:2), keeping a bath ratio of 0.1
68 g/mL. The bath was heated at 90 °C and stirred for 15 minutes. The solution was then
69 dialyzed with a membrane cell (Dialysis tubing, high retention seamless cellulose tub-
70 ing, MWCO 12400, 99.9% retention, Sigma Aldrich) for 48 hours against 1 L water.
71 Water was changed four times, and the dialysis bath was kept under magnetic stirring
72 to facilitate the desalination process. The effective elimination of the salt was verified
73 through AgNO_3 chloride assays. The dialyzed solution was centrifuged twice at 9000
74 rpm for ten minutes, and the supernatant separated. The final concentration of fibroin
75 in the dispersion (2.70% w/v) was measured gravimetrically by weighting 1000 μL of
76 dispersion before and after complete drying. The fibroin dispersion was then diluted
77 to 0.15% w/v. Aqueous CNC dispersions were prepared by magnetic stirring CNC
78 powder into water for 5 h at room temperature. The dispersions were then ultrasonified
79 for 5 minutes with 20% amplitude, using a Branson S-450 ultrasonifier equipped with
80 micro-tip. A concentration of 0.15% was prepared. SRSF/CNC hybrid dispersions
81 were prepared by mixing and magnetically stirring CNC and SRSF dispersions at the
82 moderate speed of 300 rpm, obtaining the total concentration 0.15%/0.15% w/v. The
83 prepared dispersions are neutral (pH 6.5-7.0). The selected SRSF and CNC concentra-
84 tions were found to be particularly effective in preserving aged and fragile silk textiles,
85 while avoiding gelation of CNC that prevents practical application of the dispersions.
86 Measurements were performed at different waiting times after sample preparation, as
87 detailed in section 3.

88 2.2. Rheology

89 Rheological measurements were performed with a DHR3 hybrid rheometer (TA In-
90 struments) using a 40mm smooth cone-plate geometry. Sample evaporation was found
91 to be negligible over the duration of the experiments, as determined from repeated tests
92 performed at different waiting times after sample loading. The temperature of the bot-
93 tom plate was controlled through a Peltier heating/cooling system and was set to $T =$
94 20 °C. Flow curves were measured for $10\text{ s}^{-1} < \dot{\gamma} < 500\text{ s}^{-1}$ using an equilibration
95 time of 10 s and an averaging time of 30 s. Step rate experiments were performed
96 for $\dot{\gamma} = 0.1, 0.5, 1.0, 5.0$ and 10.0 s^{-1} and creep tests for applied stresses $\sigma = 0.10,$
97 $0.30, 0.50, 0.70$ and 1.00 Pa . Dynamic frequency sweeps were measured for a strain
98 amplitude $\gamma_0 = 1.0\%$, which lies within the linear response regime, see Fig.6. Each
99 measured point is the result of averaging over 3 cycles of oscillation. Finally, Dynamic

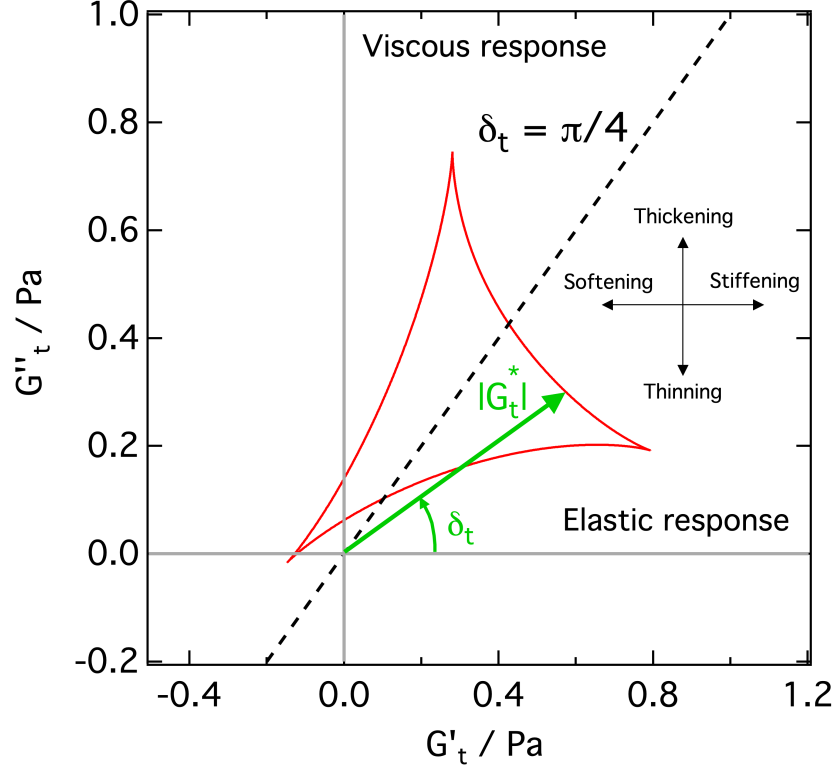


Figure 1: Exemplary Cole-Cole plot illustrating the meaning of δ_t and $|G_t^*|$, as well as the in-cycle yielding criterion. Each value along the Cole-Cole curve corresponds to a value of the instantaneous moduli, which together determine the modulus of $|G_t^*|$. δ_t quantifies the ratio between viscous and elastic contributions. When the value of $\delta_t = \pi/4$ is exceeded, the material transitions from a dominant elastic to a dominant viscous response, therefore yielding. Directions of in-cycle stiffening/softening and thickening/thinning are indicated by black arrows.

100 strain sweeps were measured for $\omega_0 = 1.0$ rad/s and increasing strain amplitude. Mea-
 101 surements at each strain amplitude were averaged over 3 cycles and the raw strain and
 102 stress signal were recorded and analyzed as described in the following section. Since
 103 the kinetics of gel formation in these samples is extremely slow, as will be shown in the
 104 Results and Discussion section, i.e. gel structures form over times considerably longer
 105 than a day, no rejuvenation protocol could be used. The different tests were thus per-
 106 formed each time on new samples having the same age with respect to the preparation
 107 time. Samples were freshly loaded following the same protocol. Error bars on the
 108 rheological data are smaller than the symbol size.

109 2.3. SPP analysis

110 During dynamic strain sweeps the raw stress and strain signals were recorded.
 111 These were later analyzed according to the SPP approach using the MATLAB-based
 112 SPPplus analysis software [32]. The SPP technique has been described in detail in
 113 previous work by Rogers and coworkers [31, 33]. We report here a brief description of
 114 the most important concepts and of the parameters used for analyzing yielding in the
 115 SRSF and SRSF/CNC samples.

116 The SPP approach describes the rheological response to oscillatory shear as a closed
 117 three-dimensional space curve in strain, rate and stress space. For each point on the
 118 curve, a Frenet-Serret frame[34, 35] can be defined by introducing a set of three or-
 119 thonormal vectors: the tangent \mathbf{T} , normal \mathbf{N} and binormal \mathbf{B} vectors, which describe
 120 the instantaneous direction of motion, the instantaneous change in direction, and the
 121 cross product of these two. The projections of the binormal vector along the strain (γ),
 122 rate ($\dot{\gamma}/\omega$) and stress (σ) axes are used to define the instantaneous moduli G'_t and G''_t :

$$G'_t = -\frac{B_\gamma}{B_\sigma} \quad (1)$$

$$G''_t = -\frac{B_{\dot{\gamma}/\omega}}{B_\sigma} \quad (2)$$

123 For a linear rheological response the trajectory in the strain, rate, stress space is planar
 124 and the instantaneous moduli are constant within a cycle of oscillation. Instead, when
 125 the response becomes non-linear, the binormal vector \mathbf{B} will change orientation during
 126 the cycle of oscillation and thus the instantaneous moduli will not any longer be con-
 127 stant and reflect the physical processes occurring in the material.

128 The instantaneous moduli of Eq.2 can be also used to define the complex instantane-
 129 ous modulus $|G_t^*|$ and the phase angle δ_t , in analogy with the commonly used linear
 130 viscoelastic moduli:

$$|G_t^*| = \sqrt{G_t'^2 + G_t''^2} \quad (3)$$

$$\delta_t = \tan^{-1}\left(\frac{G_t''}{G_t'}\right) \quad (4)$$

131 The interpretation of these parameters in terms of material yielding can be understood
 132 using Fig.1, which shows an exemplary Cole-Cole plot in which G_t'' is reported vs.
 133 G_t' for an oscillation cycle at a certain oscillation amplitude γ_0 and frequency ω . The
 134 quantity $|G_t^*|$ represents the instantaneous magnitude of the viscoelastic response.
 135 The quantity δ_t , being the ratio between the instantaneous loss and storage moduli,
 136 is a measure of the solid-like or viscous-like response of a material: small values of
 137 δ_t indicate solid-like response while large values fluid-like response. The onset of
 138 in-cycle yielding can be therefore defined as the point at which the response changes
 139 from primarily elastic, $\delta_t < \pi/4$, to primarily viscous, $\delta_t > \pi/4$. The dashed line in
 140 Fig.1 indicates the location of the yielding points in the Cole-Cole representation of the
 141 rheological data. The directions of increasing/decreasing G_t' and G_t'' indicate in-cycle
 142 stiffening/softening and thickening/thinning, respectively (Fig.1). Finally, to quantify
 143 the rate at which changes in the state of a material occur across yielding, the phase

144 angle velocity, $\dot{\delta}_t$ can be defined. Positive values of $\dot{\delta}_t$ will be associated to yielding,
 145 i.e. an increase from a small to a large value of δ_t , while negative values of $\dot{\delta}_t$ to
 146 reformation, i.e. a transition from a large to a small value of δ_t . For a sinusoidal
 147 applied deformation, $\dot{\delta}_t$ can be expressed as:

$$\dot{\delta}_t = \frac{-\omega\dot{\sigma}(\ddot{\sigma} + \omega^2\sigma)}{\ddot{\sigma} + \omega^2\dot{\sigma}^2} \quad (5)$$

148 and introducing a normalized time $\tilde{t} = \omega t$ we obtain a dimensionless form of $\dot{\delta}_t$
 149 (which instead would have dimension t^{-1}):

$$\tilde{\delta}_t = \frac{-\tilde{\sigma}(\tilde{\ddot{\sigma}} + \tilde{\sigma})}{\tilde{\ddot{\sigma}} + \tilde{\sigma}^2} \quad (6)$$

150 3. Results and Discussion

151 3.1. Continuous shear

152 3.1.1. Viscosity vs. structuring time

153 To assess the time-dependent microscopic structuring of the pure fibroin and com-
 154 posite samples, we investigated the dependency of the samples' viscosity extracted
 155 from flow curves (Fig.2a,b) on the time elapsed after sample preparation, which we
 156 call structuring time. Panel (a) of Fig.2 shows exemplary measurements obtained for
 157 samples after 11 days: while the CNC dispersion shows a Newtonian behavior with a
 158 constant viscosity, the SRSF and SRSF/CNC samples present a shear-thinning response
 159 and a yield stress. Note that for the CNC sample, data for $\dot{\gamma} < 60 \text{ s}^{-1}$ were omitted due
 160 to the large statistical noise. To monitor the evolution of the response as a function of
 161 the structuring time, we plot in panel (b) the high-shear viscosity, η_∞ , estimated from
 162 the point of the flow curve at maximum shear rate, as a function of the structuring time.
 163 For the CNC sample η_∞ does not show any significant dependence on the structuring
 164 time, indicating that the system behaves at all times as a dilute suspension. On the other
 165 hand η_∞ for the SRSF and SRSF/CNC samples shows a pronounced increase as a func-
 166 tion of the structuring time, reaching values 6-times (SRSF) and 4-times (SRSF/CNC)
 167 higher than the initial values after 15 days. The viscosity grows faster at the begin-
 168 ning for the SRSF/CNC sample, but slower at longer times, leading to a final viscosity
 169 that is lower compared to the SRSF sample. Observation of the sample structure with
 170 bright-field microscopy (Fig.2c) evidences the progressive formation of large scale ag-
 171 gregates in both samples, and the increase of structural heterogeneity. Note that for
 172 sample SRSF no clear large scale structure is developed after 5 days, while a certain
 173 structuring is already visible for SRSF/CNC, in agreement with the viscosity data. The
 174 observed structural features are characteristic of the formation of gel networks: similar
 175 structures were previously reported for SRSF samples [8]. As discussed in the intro-
 176 duction, gel formation in pure fibroin solutions is driven by initial bonding through
 177 weak interactions followed by a strong increase in the amount of β -sheet structures,
 178 which leads to a mechanically stable network. The viscosity data thus suggest that for-
 179 mation of β -sheet structures is faster in the SRSF/CNC composites than in pure SRSF
 180 solutions. To investigate this hypothesis we performed FTIR measurements right after

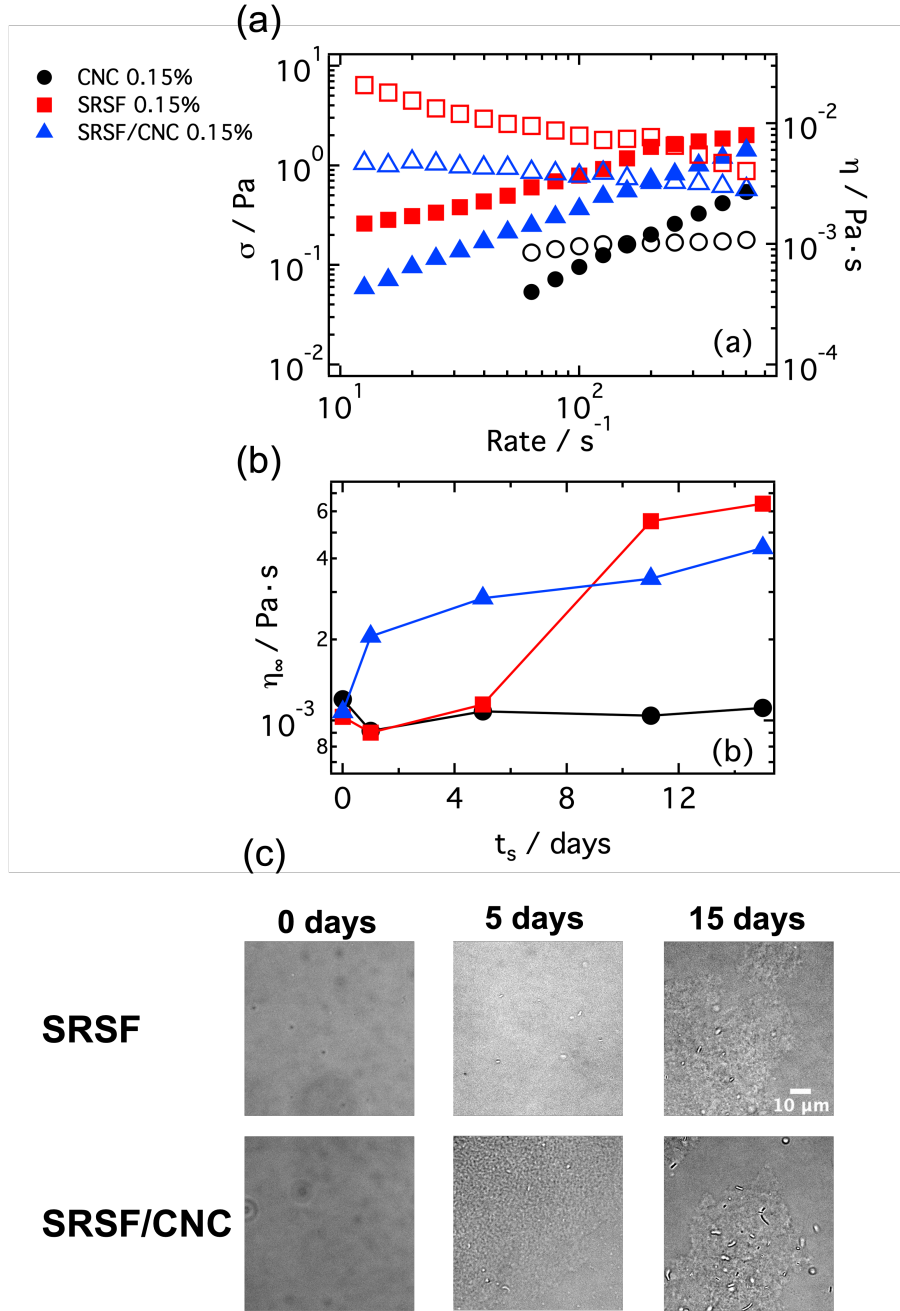


Figure 2: (a) Stress σ (left y-axis, full symbols) and viscosity η (right y-axis, open symbols) vs shear rate measured for CNC 0.15%, SRSF 0.15% and SRSF/CNC 0.15%/0.15% samples after 11 days, as indicated. (b) High shear viscosity η_{∞} extracted from flow curves, as a function of structuring time (t_s) for the same samples as in (a). (c) Bright-field microscopy snapshots illustrating the structural evolution of the samples as a function of structuring time. A scale bar, which is equal for all images, is reported in the image of the SRSF sample measured after 15 days of structuring time.

sample preparation and at the structuring time of 1 day. The results, which are reported in Fig.S1 of the Supplementary Material, show that while the amount of β -sheet structures is similar in SRSF and SRSF/CNC at 0 structuring time, it increases significantly more in SRSF/CNC, leading thus to a faster structuring. Note also that the SRSF/CNC samples present a larger amount of α -helix structures. Additional discussion of the FTIR results can be found in the Supplementary Material. Further characterization of the structure at smaller length scales of SRSF and SRSF/CNC samples after 13 days was obtained by SAXS and is reported in the Supplementary Material. The SAXS data show that the SRSF network is formed by small fractal fibroin aggregates of average size $\xi \approx 65$ nm and fractal dimension $d_m \approx 1.8$. In the SRSF/CNC the network is also formed by aggregates, however with a slightly smaller average size, $\xi \approx 14$ nm and slightly large fractal dimension, $d_m \approx 2.0$. These results confirm that the mixing with CNC alters the structural evolution of the sample and network formation.

3.1.2. Stress Growth and Creep

Stress growth and creep tests were performed to investigate the yielding under continuous shearing of the gel structures formed in the SRSF and SRSF/CNC samples after 13 days of structuring time, which correspond to steady state gel structures (no significantly different behavior is expected compared to 15 days of structuring time). Fig.3a shows the stress σ vs. strain γ curves measured for the two samples under different applied shear rates $\dot{\gamma}$ in the range $0.1 \leq \dot{\gamma} \leq 10 \text{ s}^{-1}$. Both samples show a qualitatively similar transient response characterized by an initial increase of the stress in the linear response regime followed by a stress overshoot, and later a tendency to a constant σ value characteristic of fluid flow. The stress overshoot indicates a yielding process associated with the breaking of the joints of the network structure. In colloidal gels it has been associated to bond breaking and cluster disruption [36, 37, 38, 39, 40, 41]. In our samples, the mechanical stability of the network is mainly due to the presence of β -sheet intermolecular structures, which are thus expected to break apart at the yield point. The strain at which the overshoot is observed provides therefore an estimate of the yield strain γ_y of the gel, and can be associated to a characteristic length scale in the microscopic structure of the samples. The stress at the overshoot is an estimate of the yield stress σ_y of the gel. The overshoot is observed at a strain $\gamma_y \approx 50$ % for the SRSF sample at rates $\dot{\gamma} = 1.0$ and 5.0 s^{-1} , while for $\dot{\gamma} = 10.0 \text{ s}^{-1}$ the presence of the overshoot is less clear, since for this high rate data at short times (strains) are affected by tool inertia[42]. For the SRSF/CNC samples the overshoot is observed at a comparable value γ_y for the smallest rate $\dot{\gamma} = 0.1 \text{ s}^{-1}$, but shifts to increasingly smaller values for $\dot{\gamma} = 0.5$ and 1.0 s^{-1} (Fig.4a), indicating that the sample becomes more brittle with increasing $\dot{\gamma}$. At comparable rate, the yield strain γ_y is smaller for the SRSF/CNC sample (Fig.4a), indicating a different microscopic structure of the SRSF and SRSF/CNC gels, as suggested by SAXS.

The yield stresses of both samples increase with increasing shear rate (Fig.3a, Fig.4b), indicating that breaking of the network structure needs a larger amount of energy for higher shear rates. The yield stress of the SRSF/CNC sample is slightly larger than that of the pure SRSF sample. The amount of stress stored in the system during yielding and released when the system flows can be estimated from the relative height of the stress overshoot, which we define as $(\sigma_y - \sigma_p)/\sigma_p$, with σ_p the stress in the steady state

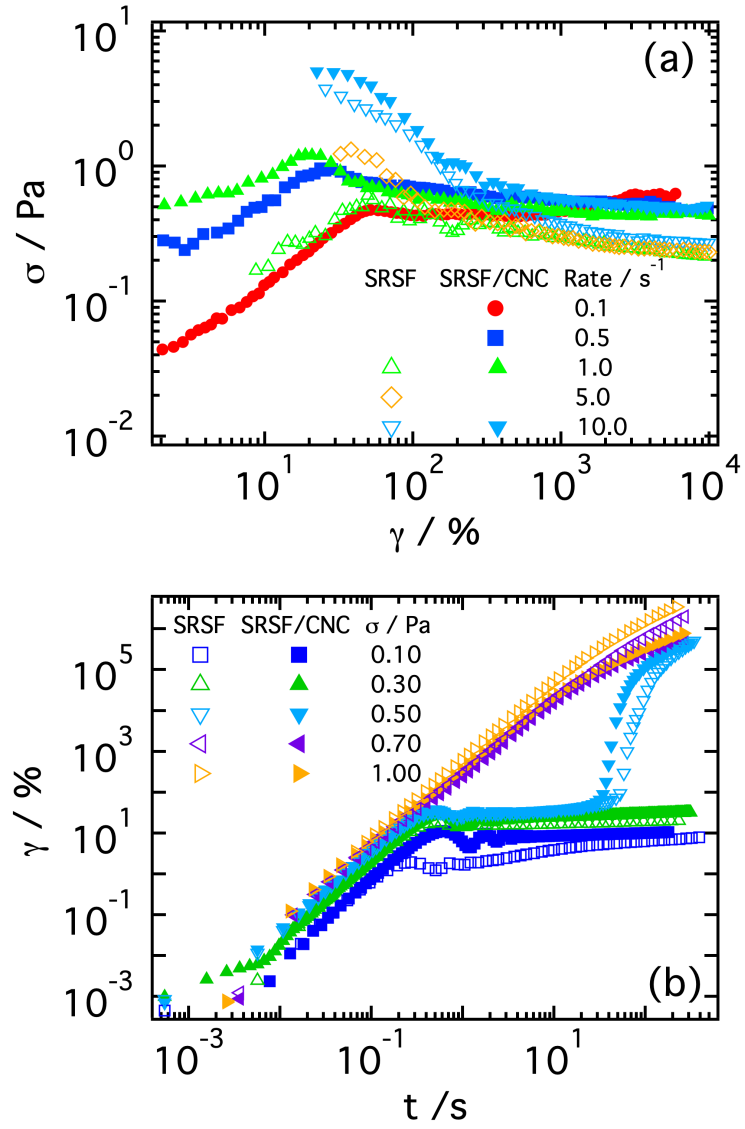


Figure 3: Stress σ vs strain γ from stress growth experiments (a) and strain γ vs. time t from creep experiments (b) performed on samples SRSF 0.15% and SRSF/CNC 0.15%/0.15% after 13 days. The applied shear rates and stresses are reported in legends.

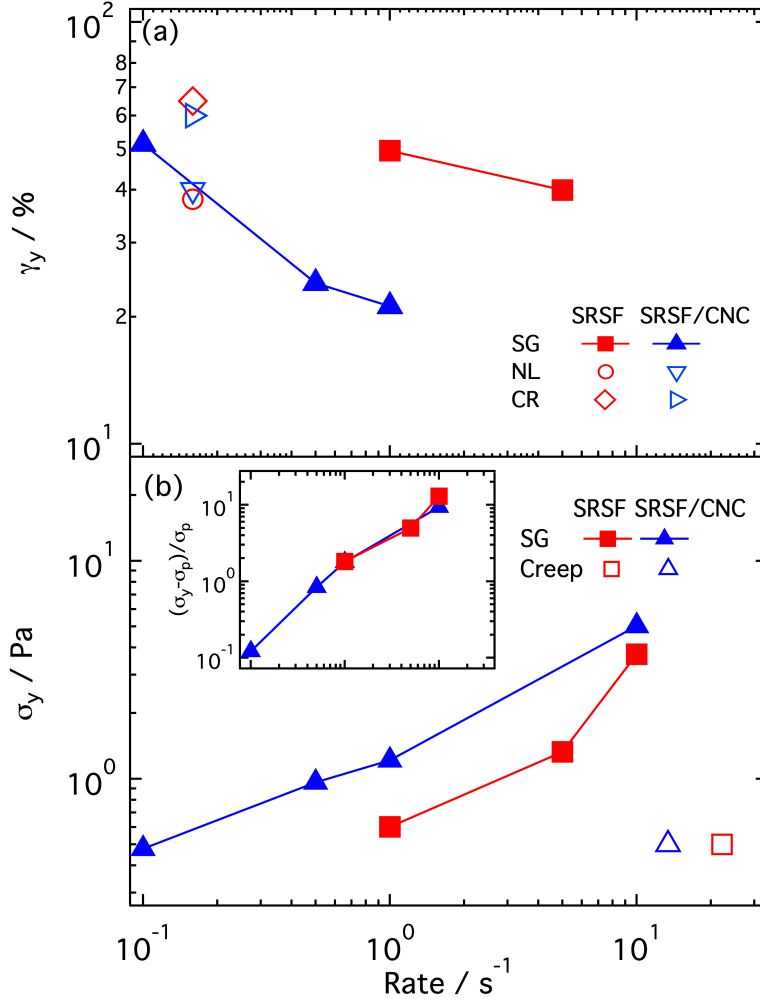


Figure 4: Yield strain γ_y (a) and yield stress σ_y (b) vs shear rate, extracted from the stress overshoot in stress growth experiments on samples SRSF 0.15% and SRSF/CNC 0.15%/0.15%. In (a) values of the yield strain obtained from the onset of non-linear regime (NL) and the crossover (CR) of the viscoelastic moduli in oscillatory dynamic strain sweeps are reported for comparison. The yield stress obtained from creep experiments is reported for comparison in panel (b) for the same samples. Inset in (b): amount of stress overshoot as a function of shear rate, same x-axis as the main plot.

of flow. The relative height of the overshoot increases with increasing rate, meaning that more stress is stored before the system yields. The two samples show comparable values of this quantity. This suggests that the larger yield stress of the SRSF/CNC sample is associated primarily to a larger elasticity of the gel network, which might be connected to changes in the aggregate size and fractal dimension evidenced by the SAXS measurements and also in recent work [43]. Measurements of the viscoelastic moduli presented in the next section confirm the increase of elasticity in the presence of CNC.

Fig.3b shows strain vs. time curves obtained from creep experiments for selected, different applied stresses. We neglect in what follows data for $t < 10^{-1}$ s, which are affected by tool inertia [44]. For small applied stresses the response of both samples is that of a creeping solid, with γ increasing slowly with increasing elapsed time t . The increase of γ is slightly slower for the SRSF sample. For large stresses the systems show a flowing behavior, with γ increasing linearly as a function of t at sufficiently long times. For intermediate stresses, like the curves for $\sigma = 0.50$ Pa in Fig.3b, a transition from creep to flow behavior is observed in the experimental time window, indicating yielding. As it can be seen the transition from creep to flow is sudden for both samples. We defined a yield stress in creep tests as the applied stress for which the strain vs. time curve shows for the first time a transition from creep to flow. The obtained values were reported in Fig.4b, using the value of the shear rate achieved when the system flows, i.e. at long times within the creep measurement. The yield stresses obtained from creep measurements are smaller than those determined from stress growth tests. This indicates that for these samples the application of stress is more effective than strain in rearranging the network structure [45].

3.2. Oscillatory shear

3.2.1. Linear Viscoelasticity

The linear viscoelastic moduli of the SRSF and SRSF/CNC gels (samples measured after 13 days) were determined by small amplitude oscillatory shear with a strain amplitude $\gamma_0 = 1\%$. They show the characteristic response of soft solid samples like gels and glasses (Fig.5a) [46, 47, 48]: the storage modulus $G'(\omega)$ is larger than the loss modulus $G''(\omega)$ for all frequencies and the gap between the moduli increases with decreasing ω . The moduli of the SRSF/CNC sample are slightly larger than those of the pure SRSF sample suggesting, as already discussed, a stiffening effect induced by the presence of the cellulose nanocrystals which lead to more compact fibroin aggregates at the nanoscale, as shown by the SAXS measurements and as observed before [43]. At the same time they present a more pronounced frequency dependence for $\omega > 1$ rad/s, which suggests that the moduli of the SRSF/CNC sample could present a crossover in the region $\omega > 40$ rad/s, at a smaller frequency compared to the SRSF sample. This different behavior might result from contributions of relaxation processes of CNC at high frequencies [49].

3.2.2. LAOS: Dynamic Strain Sweeps and Lissajous-Bowditch Plots

To explore the yielding behavior under oscillatory shear, dynamic strain sweeps at frequency $\omega_0 = 1.0$ rad/s were measured for both samples. For each strain amplitude

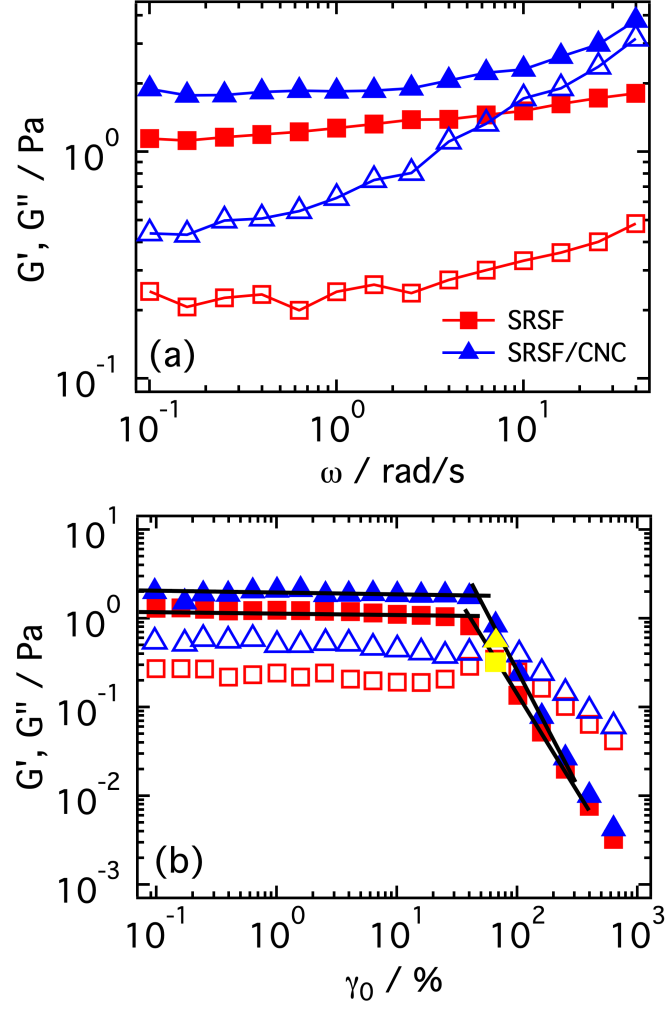


Figure 5: Storage G' and loss G'' moduli obtained for samples SRSF 0.15% and SRSF/CNC 0.15%/0.15%, for a structuring time of 13 days, as a function of (a) angular frequency ω , from SAOS measurements with $\gamma_0 = 1\%$ and (b) strain amplitude γ_0 , from LAOS measurements at a frequency $\omega_0 = 1$ rad/s. The crossing point of the solid lines in (b) indicates the extrapolation of the transition from linear to non-linear response. The yellow symbols in (b) correspond to the maximum of G'' which also coincides with the crossover between G' and G'' .

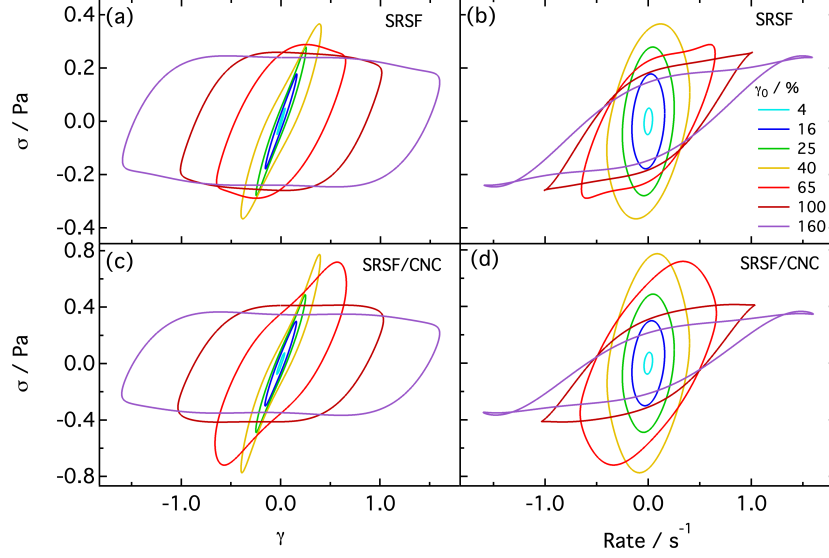


Figure 6: Elastic (a,c) and Viscous (b,d) Lissajous-Bowditch plots for samples SRSF 0.15% and SRSF/CNC 0.15%/0.15%, obtained from the raw stress, strain and strain rate signals measured in LAOS experiments with strain amplitudes $\gamma_0 = 4\%$, 16%, 25%, 40%, 65%, 100%, 160%, from cyan to purple.

value along the strain sweep, the raw stress and strain data were additionally extracted for one cycle of oscillation. Fig.5b shows the amplitude-dependent moduli obtained in harmonic approximation directly from the rheometer. Additional analysis considering anharmonic contributions to the stress in the non-linear response regime will be presented in the next section. The moduli $G'(\gamma_0)$ and $G''(\gamma_0)$ obtained in harmonic approximation show a constant value in the linear viscoelastic response regime, followed by a decrease of G' and a simultaneous increase of G'' . The onset of decrease of G' has been often used to define a yield strain γ_y^{NL} [36, 50, 51]. The two moduli reach a crossover, which also roughly coincides with the maximum of G'' . This crossover corresponds apparently to the transition from solid-like to fluid-like response and to maximum dissipation (maximum of G''), and defines an alternative value for the yield strain γ_y^{CR} [52, 36, 50]. After the crossover, both moduli decrease as a function of increasing γ_0 , following the fluidization of the sample. The values of γ_y^{NL} and γ_y^{CR} for the two samples are reported in Fig.4a: γ_y^{NL} is closely comparable to the yield strain estimated from step rate experiments, while γ_y^{CR} is larger. This suggests that significant network structure rearrangement takes place already at the onset of non-linear response: this will be confirmed by the SPP analysis. Additionally, at large amplitudes γ_0 the storage modulus $G' \sim \gamma_0^v$, with $v \approx -2.2$ for the SRSF sample, and $v \approx -2.3$ for the SRSF/CNC sample. According to recent work, for a slope $v = -2$ there is a constant average amount of energy stored per cycle [53]. Above yielding, any additional energy input is dissipated to the environment and does not contribute to internal

290 rearrangement of the structure. This suggests that the most energetically efficient flow
 291 condition can be obtained just above yielding, a result which shows analogies with the
 292 behavior of glassy mixtures of hard spheres [45].
 293 Fig.6 shows elastic and viscous Lissajous-Bowditch curves [54, 55] extracted from the
 294 raw stress and strain signals measured within a cycle of oscillation for different strain
 295 amplitudes γ_0 . Within the linear response regime the Lissajous-Bowditch figures of
 296 a viscoelastic material are expected to be elliptical and any deviation from the ellipti-
 297 cal shape indicates the presence of higher-order harmonics in the response. We can
 298 observe that for $\gamma_0 = 4\%$ and 16% both elastic and viscous figures are indeed ellipti-
 299 cal, confirming that the response is linear for these values of the strain amplitude. For
 300 $\gamma_0 = 25\%$ slight deviations from the elliptical shape are already visible: in particular
 301 in the elastic figure approaching the maximum strain amplitude, where shear reversal
 302 occurs, the stress increases in a slightly super-linear fashion, indicating the presence
 303 of strain hardening. For $\gamma_0 = 40\%$ the hardening response is further enhanced. Strain
 304 hardening effects have been observed in pure fibroin solutions with concentrations \gtrsim
 305 4% [10, 11, 12], and have been attributed to the shear-induced formation of transient
 306 intermolecular domains that act as additional cross-links [13]. While the concentration
 307 in our samples is much lower, at the extreme of the oscillation amplitude, before net-
 308 work yielding, this kind of phenomena may start to appear. When $\gamma_0 = 65\%$, while the
 309 response is still qualitatively similar for sample SRSF/CNC, it changes significantly
 310 for the pure SRSF sample: in the elastic figure, well before strain reversal the stress
 311 first flattens and then decreases presenting a maximum or overshoot similar to that ob-
 312 served in the stress growth experiments. In the viscous figure, the stress first flattens
 313 indicating shear thinning, which apparently is interrupted before shear reversal, since
 314 σ slightly increases as a function of $\dot{\gamma}$. For the two largest values of $\gamma_0 = 100\%$ and
 315 160% the response indicates that the system flows over a large portion of the cycle, as
 316 indicated by the almost constant stress in the elastic figure. The flat parts in the viscous
 317 figure correspond to shear thinning behavior.

318 3.2.3. LAOS: SPP Analysis

319 The SPP analysis allows to get more detailed insight into the yielding transition
 320 under oscillatory shear, providing information on the dynamics of the mechanical re-
 321 sponse during a cycle of oscillation. Figs.7a,b show Cole-Cole plots of the instanta-
 322 neous moduli G'_t and G''_t for selected values of the strain amplitude $\gamma_0 = 25\%$, 40% ,
 323 65% , 100% and 160% . For $\gamma_0 = 25\%$ the curve for the SRSF samples lies almost en-
 324 tirely in the region below the $\delta_t = \pi/4$ line and therefore the sample response is still
 325 predominantly elastic over the entire oscillation cycle. The data for the SRSF/CNC
 326 samples lie even deeper inside the elastic region. When $\gamma_0 = 40\%$ the response of the
 327 two samples shows a marked difference: for the SRSF sample a large part of the curve
 328 lies above the $\delta_t = \pi/4$ line, i.e. the sample yields and is fluidized for a large portion
 329 of the cycle; the response of the SRSF/CNC sample instead still lies almost entirely
 330 within the elastic region. For larger values of γ_0 increasingly larger portions of the
 331 curves lie within the viscous region in correspondence to the progressive fluidization
 332 of the samples within a cycle. As it can be noticed, the fluidization of the SRSF/CNC
 333 sample is delayed in terms of strain amplitude compared to the SRSF sample. A yield
 334 strain value can be estimated as the smallest value of the strain amplitude for which

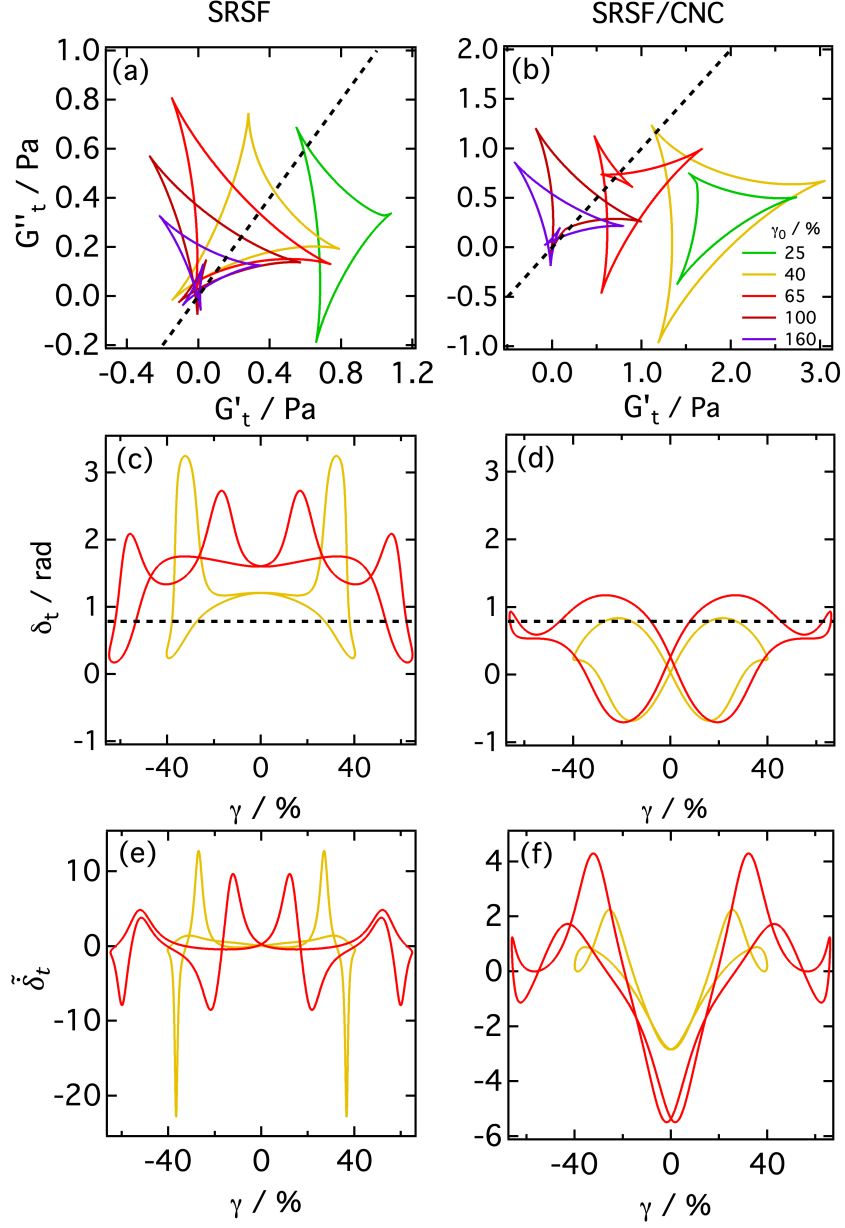


Figure 7: (a),(b) Cole-Cole plot of the instantaneous moduli G'_t and G''_t (c),(d) instantaneous phase angle δ_t vs. strain γ , (e),(f) phase angle velocity $\dot{\delta}_t$ vs. strain, obtained from SPP analysis applied to samples SRSF 0.15% (a,c,e) and SRSF/CNC 0.15%/0.15% (b,d,f).

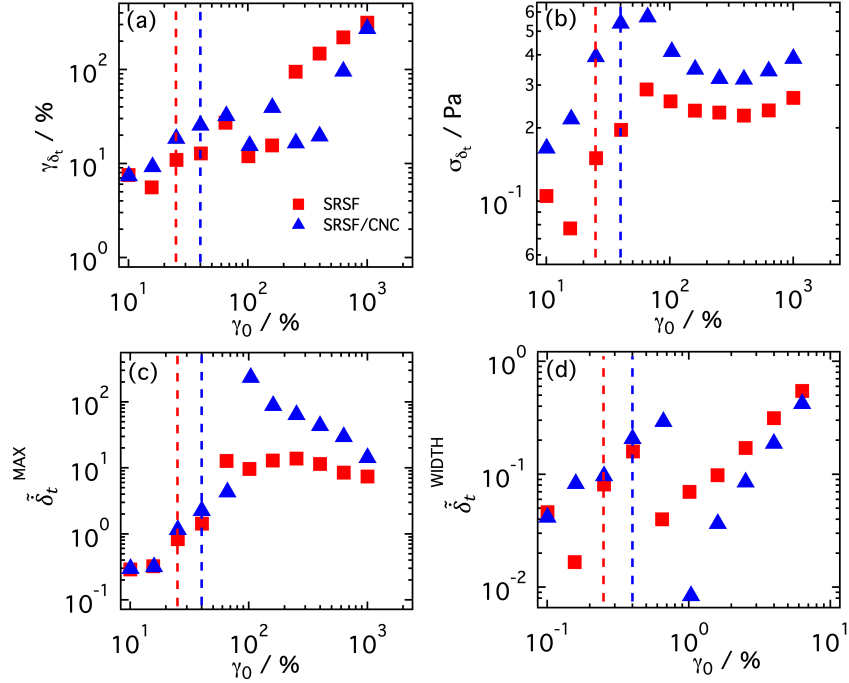


Figure 8: (a) Strain γ_{δ_t} and (b) stress σ_{δ_t} at which the primary maxima of $\tilde{\delta}_t$ are observed, and the corresponding height $\tilde{\delta}_t^{MAX}$ and width $\tilde{\delta}_t^{WIDTH}$ of the peaks, as a function of strain amplitude γ_0 , for samples SRSF 0.15% and SRSF/CNC 0.15%/0.15%, as indicated. Dashed lines indicate the yield strain estimated from the Cole-Cole plots for the two samples.

at least a portion of the curve first crosses the $\delta_t = \pi/4$ line. According to this definition, we obtain values of $\gamma_y^{CC} = 25\%$ and 40% for samples SRSF and SRSF/CNC, respectively. These are smaller (SRSF) or comparable (SRSF/CNC) to the yield strain estimated as the onset of non-linearity in the moduli calculated in harmonic approximation. This result shows that already at the onset of non-linear response indicated by the moduli extracted in harmonic approximation, partial fluidization is present during a cycle of deformation. However, the average moduli calculated in harmonic approximation reflect the dominant response during a cycle. This confirms that only a detailed analysis of the in-cycle response allows to precisely identify the onset of fluidization. An additional estimate of the recoverable yield strain could be obtained in the limit of $G'_t \gg G''_t$ for large values of the strain amplitude[32], through the estimate of the elastic strain $\gamma_{el} \approx \sigma/G'_t$. Performing this calculation for the vertices with the highest G'_t value of the Cole-Cole diagrams in Fig.7 for $\gamma_0 = 100\%$ and 160% we obtained $\gamma_{el} \approx 17\%$ for SRSF and $\gamma_{el} \approx 20\%$ for SRSF/CNC, comparable but slightly smaller than the yield strains obtained in harmonic approximation.

Fig.7 reports in addition plots of the phase angle δ_t (panels c,d) and phase angle velocity $\tilde{\delta}_t$ (panels e,f) as a function of γ , for strain amplitudes $\gamma_0 = 40\%$ and 65% ,

352 i.e. close to the yielding transition determined from the Cole-Cole analysis. Similar to
 353 what was discussed for Figs.7a,b, in cycle yielding occurs when $\delta_t > \pi/4$. Moreover,
 354 peaks in the phase angle correspond to largest ratios G_t''/G_t' and therefore indicate the
 355 maximal fluidization of the samples. The results in Figs.7c,d show that this occurs be-
 356 fore the maximum strain amplitude is reached, and that for the SRSF sample, which
 357 presents a larger fluidization at comparable strain amplitude, it shifts to increasingly
 358 smaller values of γ . The peaks are relatively narrow and large for sample SRSF, while
 359 broad and small for sample SRSF/CNC.

360 The phase angle velocities $\dot{\delta}_t$ in Figs.7e,f are used to estimate the dynamics of the yield-
 361 ing transition around the peaks of δ_t . The positive peaks of $\dot{\delta}_t$, indicative of the main
 362 yielding transition, are particularly pronounced for sample SRSF and strain amplitude
 363 of 40%. The same data also show a rapid reformation of the sample structure after
 364 shear reversal (negative peaks).

365 We analysed in more detail the dynamics of yielding by extracting the values of the
 366 strain (γ_{δ_t}) and stress (σ_{δ_t}) at the main positive peaks of the $\dot{\delta}_t$ curves, as well as the
 367 height ($\dot{\delta}_t^{MAX}$) and width ($\dot{\delta}_t^{WIDTH}$) of the same peaks. Fig.8 shows these values as a
 368 function of the applied strain amplitude γ_0 .

369 The in-cycle yield strain γ_{δ_t} is seen to increase initially with increasing γ_0 until $\gamma_0 =$
 370 65%: for larger values up to 160% or 300%, for SRSF and SRSF/CNC respectively, γ_{δ_t}
 371 remains approximately constant, with moderate fluctuations between $20\% < \gamma_{\delta_t} < 30\%$
 372 (Fig.8a). For even larger γ_0 the values of γ_{δ_t} increase again. Note that $\gamma_0 = 65\%$ approx-
 373 imately corresponds to the strain amplitude at which a crossover between the moduli
 374 calculated in harmonic approximation, G' and G'' , is observed. It is also the value for
 375 which a larger portion of the curves in the Cole-Cole plot occupies the viscous region.
 376 This result suggests therefore that there is a characteristic value of the in-cycle strain
 377 at which fluidization starts, $\gamma_{\delta_t}^* \approx 20\text{-}30\%$, and that above the crossover amplitude this
 378 value remains constant for a broad interval of strain amplitudes. Note that a strain
 379 amplitude of about 30% also corresponds to the onset of non-linear response in the
 380 amplitude sweeps, see Fig.5. This suggests that the in-cycle yielding is responsible
 381 for the increase in energy dissipation and the decrease of energy storage observed in
 382 the harmonic approximation. When the sample at the beginning of the test is already
 383 almost fluid, the value of γ_{δ_t} moves closer to the maximum strain amplitude. The stress
 384 corresponding to the peak of $\dot{\delta}_t$ shows even more clearly the qualitative change in the
 385 response of the gels around $\gamma_0 = 65\%$ (Fig.8b): For this value a maximum of σ_{δ_t} is
 386 found, similar to the stress overshoot in stress growth experiments. Thus stress ac-
 387 cumulation grows until fluid-like behavior becomes dominant over a single cycle and
 388 later decays according to an almost complete fluidization of the sample. In the flu-
 389 idized sample σ_{δ_t} is approximately constant. The height of the peak, $\dot{\delta}_t^{MAX}$, is also
 390 growing up to the same characteristic value and then remains constant (SRSF) or de-
 391 creases (SRSF/CNC). This tells us that the velocity of the transition increases up to
 392 $\gamma_0 = 65\%$ and then stabilizes since the sample is already fluid-like. Interestingly, the
 393 width of the peak, $\dot{\delta}_t^{WIDTH}$, which indicates how broad is the transition in terms of
 394 applied strain amplitude, presents instead a discontinuity around the same value of γ_0 :
 395 the width grows up to that value, then it suddenly drops and finally increases again.

396 This behavior is reminiscent of a first order transition [56]. Summarizing, the onset of
 397 non-linear response in harmonic approximation roughly coincides with the first value
 398 of γ_0 for which a small portion of the cycle presents a predominantly viscous response.
 399 Instead, the crossing of G' and G'' is instead comparable to the value of γ_0 for which,
 400 for the first time, the majority of the cycle is predominantly viscous. i.e the sample is
 401 completely fluidized.

402 4. Conclusions

403 We investigated the mechanical response of gels formed by self-regenerated silk fi-
 404 broin and its mixture with cellulose nano-crystals, with a particular focus on the yield-
 405 ing transition. Measurements of the high shear viscosity as a function of structuring
 406 time show that the gelation kinetics become faster with addition of CNC: comparison
 407 with FTIR data shows that this is the result of the formation of a larger fraction of β -
 408 sheet structures in the SRSF/CNC composites. At the end of the structuring time both
 409 gels present weak solid structures characterized by storage moduli and yield stresses of
 410 the order of Pas, with both quantities being slightly larger for the SRSF/CNC gel. The
 411 larger storage modulus and yield stress of the SRSF/CNC gel can be associated with
 412 the formation of more compact fibroin aggregates at the nanoscale and to a larger con-
 413 tent of β -sheet structures. We additionally found that while the yield stress increases
 414 with increasing $\dot{\gamma}$, the yield strain decreases. We speculate that this indicates a shear-
 415 induced compaction of β -sheet bonding structures at higher shear rates, which need a
 416 larger stress but smaller strain to be broken.

417 The analysis of the yielding process from LAOS measurements in first harmonic ap-
 418 proximation allows to extract two distinct estimates of the yield strain: one correspond-
 419 ing to the onset of non-linear response, at $\gamma_y \approx 40\%$, which is comparable to results of
 420 step rate tests, and a second to the crossover of G' and G'' , at $\gamma_y \approx 65\%$. A detailed
 421 analysis of the in-cycle yielding through the SPP approach, sheds light on the dif-
 422 ference between these two estimates: the onset of non-linear response is the point at
 423 which the fluidization process begins, while the crossing of G' and G'' is the end of
 424 the process, corresponding to a major fluidization of the sample which is reflected in a
 425 stress maximum and a maximum velocity and width of the solid-fluid yielding transi-
 426 tion. The entire fluidization process thus spans a broad range of strain amplitudes. The
 427 SPP analysis also reveals that when the system becomes predominantly viscous (for
 428 $\gamma_0 > 65\%$), the onset of the solid-fluid transition always occurs at a similar in-cycle
 429 strain of about 20-30%. Our study evidences that a detailed analysis of the mechan-
 430 ical properties and yielding behavior of complex gel structures, like those formed by
 431 SRSF/CNC dispersions, is of fundamental importance to design adequate processing
 432 conditions in applications, such as the consolidation of silk artworks.

433 Acknowledgments

434 We thank S. Rogers for providing the codes for the SPP analysis and for stimulating
 435 discussions. We acknowledge financial support from CSGI.

436 Data Availability Statement

437 The data that support the findings of this study are available from the corresponding
438 author upon reasonable request.

439 References

- 440 [1] T. Biswal, S. K. Badjena, D. Pradhan, Sustainable biomaterials and their
441 applications: A short review, *Mater. Today: Proc.* 30 (2020) 274–282,
442 national Conference on “Trends in Minerals & Materials Technology”.
443 doi:<https://doi.org/10.1016/j.matpr.2020.01.437>.
444 URL [https://www.sciencedirect.com/science/article/pii/](https://www.sciencedirect.com/science/article/pii/S2214785320305423)
445 [S2214785320305423](https://www.sciencedirect.com/science/article/pii/S2214785320305423)
- 446 [2] H. S. Shekar, M. Ramachandra, Green composites: A review, *Mater. Today: Proc.*
447 5 (1, Part 3) (2018) 2518–2526, international Conference on Advanced Materials
448 and Applications (ICAMA 2016), June 15-17, 2016, Bengaluru, Karanataka,
449 INDIA. doi:<https://doi.org/10.1016/j.matpr.2017.11.034>.
450 URL [https://www.sciencedirect.com/science/article/pii/](https://www.sciencedirect.com/science/article/pii/S2214785317322666)
451 [S2214785317322666](https://www.sciencedirect.com/science/article/pii/S2214785317322666)
- 452 [3] M. A. Meyers, P.-Y. Chen, A. Y.-M. Lin, Y. Seki, Biological materials:
453 Structure and mechanical properties, *Prog. Mater. Sci.* 53 (1) (2008) 1–206.
454 doi:<https://doi.org/10.1016/j.pmatsci.2007.05.002>.
455 URL [https://www.sciencedirect.com/science/article/pii/](https://www.sciencedirect.com/science/article/pii/S0079642507000254)
456 [S0079642507000254](https://www.sciencedirect.com/science/article/pii/S0079642507000254)
- 457 [4] M. P. Dicker, P. F. Duckworth, A. B. Baker, G. Francois, M. K. Hazzard,
458 P. M. Weaver, Green composites: A review of material attributes and com-
459plementary applications, *Compos. - A: Appl. Sci. Manuf.* 56 (2014) 280–289.
460 doi:<https://doi.org/10.1016/j.compositesa.2013.10.014>.
461 URL [https://www.sciencedirect.com/science/article/pii/](https://www.sciencedirect.com/science/article/pii/S1359835X13002893)
462 [S1359835X13002893](https://www.sciencedirect.com/science/article/pii/S1359835X13002893)
- 463 [5] J. Gosline, P. Guerette, C. Ortlepp, K. Savage, The mechanical design of
464 spider silks: from fibroin sequence to mechanical function, *J. Exp. Biol.*
465 202 (23) (1999) 3295–3303. arXiv:[https://journals.biologists.com/](https://journals.biologists.com/jeb/article-pdf/202/23/3295/1235956/3295.pdf)
466 [jeb/article-pdf/202/23/3295/1235956/3295.pdf](https://journals.biologists.com/jeb/article-pdf/202/23/3295/1235956/3295.pdf), doi:10.1242/jeb.
467 202.23.3295.
468 URL <https://doi.org/10.1242/jeb.202.23.3295>
- 469 [6] X. Qiao, R. Miller, E. Schneck, K. Sun, Foaming properties and the
470 dynamics of adsorption and surface rheology of silk fibroin at the
471 air/water interface, *Coll. Surf. A* 591 (2020) 124553. doi:<https://doi.org/10.1016/j.colsurfa.2020.124553>.
472 URL [https://www.sciencedirect.com/science/article/pii/](https://www.sciencedirect.com/science/article/pii/S0927775720301461)
473 [S0927775720301461](https://www.sciencedirect.com/science/article/pii/S0927775720301461)
474

- 475 [7] A. Matsumoto, J. Chen, A. L. Collette, U.-J. Kim, G. H. Altman, P. Cebe, D. L.
476 Kaplan, Mechanisms of silk fibroin solgel transitions, *J. Phys. Chem. B* 110
477 (2006) 21630–21638. doi:10.1021/jp056350v.
478 URL <https://doi.org/10.1021/jp056350v>
- 479 [8] S. Kapoor, S. C. Kundu, Silk protein-based hydrogels: Promising advanced
480 materials for biomedical applications, *Acta Biomater.* 31 (2016) 17–32.
481 doi:<https://doi.org/10.1016/j.actbio.2015.11.034>.
482 URL [https://www.sciencedirect.com/science/article/pii/](https://www.sciencedirect.com/science/article/pii/S1742706115302105)
483 [S1742706115302105](https://www.sciencedirect.com/science/article/pii/S1742706115302105)
- 484 [9] S. Nagarkar, A. Patil, A. Lele, S. Bhat, J. Bellare, R. A. Mashelkar, Some mech-
485 anistic insights into the gelation of regenerated silk fibroin sol, *Ind. amp; Eng.*
486 *Chem. Res.* 48 (17) (2009) 8014–8023. doi:10.1021/ie801723f.
487 URL <https://doi.org/10.1021/ie801723f>
- 488 [10] A. Matsumoto, A. Lindsay, B. Abedian, D. L. Kaplan, Silk fibroin solution prop-
489 erties related to assembly and structure, *Macromol. Biosci.* 8 (11) (2008) 1006–
490 1018. arXiv:[https://onlinelibrary.wiley.com/doi/pdf/10.1002/](https://onlinelibrary.wiley.com/doi/pdf/10.1002/mabi.200800020)
491 [mabi.200800020](https://onlinelibrary.wiley.com/doi/pdf/10.1002/mabi.200800020), doi:<https://doi.org/10.1002/mabi.200800020>.
492 URL [https://onlinelibrary.wiley.com/doi/abs/10.1002/mabi.](https://onlinelibrary.wiley.com/doi/abs/10.1002/mabi.200800020)
493 [200800020](https://onlinelibrary.wiley.com/doi/abs/10.1002/mabi.200800020)
- 494 [11] X. Chen, D. P. Knight, F. Vollrath, Rheological Characterization of Nephila
495 Spidroin Solution, *Biomacromolecules* 3 (4) (2002) 644–648. doi:10.1021/
496 bm0156126.
497 URL <https://doi.org/10.1021/bm0156126>
- 498 [12] A. Ochi, K. S. Hossain, J. Magoshi, N. Nemoto, Rheology and Dynamic Light
499 Scattering of Silk Fibroin Solution Extracted from the Middle Division of Bom-
500 byx mori Silkworm, *Biomacromolecules* 3 (6) (2002) 1187–1196. doi:10.
501 1021/bm020056g.
502 URL <https://doi.org/10.1021/bm020056g>
- 503 [13] Z. Oztoprak, O. Okay, Reversibility of strain stiffening in silk fi-
504 broin gels, *Int. J. Biol. Macromol.* 95 (2017) 24–31. doi:<https://doi.org/10.1016/j.ijbiomac.2016.11.034>.
505 URL [https://www.sciencedirect.com/science/article/pii/](https://www.sciencedirect.com/science/article/pii/S0141813016310017)
506 [S0141813016310017](https://www.sciencedirect.com/science/article/pii/S0141813016310017)
507
- 508 [14] A. P. Tabatabai, D. L. Kaplan, D. L. Blair, Rheology of reconstituted silk fibroin
509 protein gels: the epitome of extreme mechanics, *Soft Matter* 11 (2015) 756–761.
510 doi:10.1039/C4SM02079K.
511 URL <http://dx.doi.org/10.1039/C4SM02079K>
- 512 [15] U.-J. Kim, J. Park, C. Li, H.-J. Jin, R. Valluzzi, D. L. Kaplan, Structure and
513 Properties of Silk Hydrogels, *Biomacromolecules* 5 (3) (2004) 786–792. doi:
514 10.1021/bm0345460.
515 URL <https://doi.org/10.1021/bm0345460>

- [16] A. Motta, C. Migliaresi, F. Faccioni, P. Torricelli, M. Fini, R. Giardino, Fibroin hydrogels for biomedical applications: preparation, characterization and in vitro cell culture studies, *J. Biomater. Sci. Polym. Ed.* 15 (7) (2004) 851–864. doi: 10.1163/1568562041271075.
URL <https://doi.org/10.1163/1568562041271075>
- [17] B. B. Mandal, S. Kapoor, S. C. Kundu, Silk fibroin/polyacrylamide semi-interpenetrating network hydrogels for controlled drug release, *Biomaterials* 30 (14) (2009) 2826–2836. doi:<https://doi.org/10.1016/j.biomaterials.2009.01.040>.
URL <https://www.sciencedirect.com/science/article/pii/S0142961209000908>
- [18] J. Kundu, L. A. Poole-Warren, P. Martens, S. C. Kundu, Silk fibroin/poly(vinyl alcohol) photocrosslinked hydrogels for delivery of macromolecular drugs, *Acta Biomater.* 8 (5) (2012) 1720–1729. doi:<https://doi.org/10.1016/j.actbio.2012.01.004>.
URL <https://www.sciencedirect.com/science/article/pii/S1742706112000116>
- [19] J. Hu, B. Chen, F. Guo, J. Du, P. Gu, X. Lin, W. Yang, H. Zhang, M. Lu, Y. Huang, G. Xu, Injectable silk fibroin/polyurethane composite hydrogel for nucleus pulposus replacement, *J. Mater. Sci.: Mater. Med.* 23 (3) (2012) 711–722. doi:10.1007/s10856-011-4533-y.
URL <https://doi.org/10.1007/s10856-011-4533-y>
- [20] Q. Lv, K. Hu, Q. Feng, F. Cui, Fibroin/collagen hybrid hydrogels with crosslinking method: Preparation, properties, and cytocompatibility, *J. Biomed. Mater. Res.* 84A (1) (2008) 198–207. doi:<https://doi.org/10.1002/jbm.a.31366>.
URL <https://doi.org/10.1002/jbm.a.31366>
- [21] X. Chen, W. Li, W. Zhong, Y. Lu, T. Yu, pH sensitivity and ion sensitivity of hydrogels based on complex-forming chitosan/silk fibroin interpenetrating polymer network, *J. App. Polym. Sci.* 65 (11) (1997) 2257–2262. doi:[https://doi.org/10.1002/\(SICI\)1097-4628\(19970912\)65:11<2257::AID-APP23>3.0.CO;2-Z](https://doi.org/10.1002/(SICI)1097-4628(19970912)65:11<2257::AID-APP23>3.0.CO;2-Z).
URL [https://doi.org/10.1002/\(SICI\)1097-4628\(19970912\)65:11%3C2257::AID-APP23%3E3.0.COhttp://2-z](https://doi.org/10.1002/(SICI)1097-4628(19970912)65:11%3C2257::AID-APP23%3E3.0.COhttp://2-z)
- [22] K. Numata, S. Yamazaki, T. Katashima, J.-A. Chuah, N. Naga, T. Sakai, Silk-Pectin Hydrogel with Superior Mechanical Properties, Biodegradability, and Biocompatibility, *Macromol. Biosci.* 14 (6) (2014) 799–806. doi:<https://doi.org/10.1002/mabi.201300482>.
URL <https://doi.org/10.1002/mabi.201300482>
- [23] K. Ziv, H. Nuhn, Y. Ben-Haim, L. S. Sasportas, P. J. Kempen, T. P. Niedringhaus, M. Hrynyk, R. Sinclair, A. E. Barron, S. S. Gambhir, A tunable silk–alginate hydrogel scaffold for stem cell culture and

- transplantation, *Biomaterials* 35 (12) (2014) 3736–3743. doi:<https://doi.org/10.1016/j.biomaterials.2014.01.029>.
URL <https://www.sciencedirect.com/science/article/pii/S0142961214000313>
- [24] J. Huang, L. Liu, J. Yao, Electrospinning of *Bombyx mori* silk fibroin nanofiber mats reinforced by cellulose nanowhiskers, *Fibers Polym.* 12 (8) (2011) 1002–1006. doi:[10.1007/s12221-011-1002-7](https://doi.org/10.1007/s12221-011-1002-7).
URL <https://doi.org/10.1007/s12221-011-1002-7>
- [25] Y. Feng, X. Li, M. Li, D. Ye, Q. Zhang, R. You, W. Xu, Facile Preparation of Biocompatible Silk Fibroin/Cellulose Nanocomposite Films with High Mechanical Performance, *ACS Sustain. Chem. Eng.* 5 (7) (2017) 6227–6236. doi:[10.1021/acssuschemeng.7b01161](https://doi.org/10.1021/acssuschemeng.7b01161).
URL <https://doi.org/10.1021/acssuschemeng.7b01161>
- [26] J. Chen, A. Zhuang, H. Shao, X. Hu, Y. Zhang, Robust silk fibroin/bacterial cellulose nanoribbon composite scaffolds with radial lamellae and intercalation structure for bone regeneration, *J. Mater. Chem. B* 5 (20) (2017) 3640–3650. doi:[10.1039/C7TB00485K](https://doi.org/10.1039/C7TB00485K).
URL <http://dx.doi.org/10.1039/C7TB00485K>
- [27] P. Dorishetty, R. Balu, S. S. Athukoralalage, T. L. Greaves, J. Mata, L. de Campo, N. Saha, A. C. W. Zannettino, N. K. Dutta, N. R. Choudhury, Tunable Biomimetic Hydrogels from Silk Fibroin and Nanocellulose, *ACS Sustain. Chem. Eng.* 8 (6) (2020) 2375–2389. doi:[10.1021/acssuschemeng.9b05317](https://doi.org/10.1021/acssuschemeng.9b05317).
URL <https://doi.org/10.1021/acssuschemeng.9b05317>
- [28] R. Xiong, H. S. Kim, S. Zhang, S. Kim, V. F. Korolovych, R. Ma, Y. G. Yingling, C. Lu, V. V. Tsukruk, Template-Guided Assembly of Silk Fibroin on Cellulose Nanofibers for Robust Nanostructures with Ultrafast Water Transport, *ACS Nano* 11 (12) (2017) 12008–12019. doi:[10.1021/acsnano.7b04235](https://doi.org/10.1021/acsnano.7b04235).
URL <https://doi.org/10.1021/acsnano.7b04235>
- [29] D. Badillo-Sanchez, D. Chelazzi, R. Giorgi, A. Cincinelli, P. Baglioni, Characterization of the secondary structure of degummed *Bombyx mori* silk in modern and historical samples, *Polym. Degrad. Stab.* 157 (2018) 53–62. doi:<https://doi.org/10.1016/j.polymdegradstab.2018.09.022>.
URL <https://www.sciencedirect.com/science/article/pii/S0141391018303021>
- [30] D. Chelazzi, D. Badillo-Sanchez, R. Giorgi, A. Cincinelli, P. Baglioni, Self-regenerated silk fibroin with controlled crystallinity for the reinforcement of silk, *J. Coll. Interf. Sci.* 576 (2020) 230–240. doi:<https://doi.org/10.1016/j.jcis.2020.04.114>.
URL <https://www.sciencedirect.com/science/article/pii/S0021979720305786>

- [31] S. A. Rogers, In search of physical meaning: defining transient parameters for nonlinear viscoelasticity, *Rheol. Acta* 56 (5) (2017) 501–525. doi:10.1007/s00397-017-1008-1.
URL <https://doi.org/10.1007/s00397-017-1008-1>
- [32] G. J. Donley, J. R. de Bruyn, G. H. McKinley, S. A. Rogers, Time-resolved dynamics of the yielding transition in soft materials, *J. Non-Newton. Fluid Mech.* 264 (2019) 117–134. doi:<https://doi.org/10.1016/j.jnnfm.2018.10.003>.
URL <https://www.sciencedirect.com/science/article/pii/S0377025718302155>
- [33] S. A. Rogers, A sequence of physical processes determined and quantified in LAOS: An instantaneous local 2D/3D approach, *J. Rheol.* 56 (5) (2012) 1129–1151. doi:10.1122/1.4726083.
URL <https://doi.org/10.1122/1.4726083>
- [34] F. Frenet, Sur les courbes à double courbure., *J. Math. Pures Appl.* (1852) 437–447.
URL <http://eudml.org/doc/233946>
- [35] J.-A. Serret, Sur quelques formules relatives à la théorie des courbes à double courbure., *J. Math. Pures Appl.* (1851) 193–207.
URL <http://eudml.org/doc/235002>
- [36] M. Laurati, S. U. Egelhaaf, G. Petekidis, Nonlinear rheology of colloidal gels with intermediate volume fraction, *J. Rheol.* 55 (3) (2011) 673–706. doi:<http://dx.doi.org/10.1122/1.3571554>.
- [37] M. Laurati, S. U. Egelhaaf, G. Petekidis, Plastic rearrangements in colloidal gels investigated by LAOS and LS-Echo, *J. Rheol.* 58 (5) (2014) 1395–1417. doi:10.1122/1.4872059.
URL <https://doi.org/10.1122/1.4872059>
- [38] N. Koumakis, G. Petekidis, Two step yielding in attractive colloids: transition from gels to attractive glasses, *Soft Matter* 7 (2011) 2456–2470. doi:10.1039/C0SM00957A.
URL <http://dx.doi.org/10.1039/C0SM00957A>
- [39] N. Koumakis, E. Moghimi, R. Besseling, W. C. K. Poon, J. F. Brady, G. Petekidis, Tuning colloidal gels by shear, *Soft Matter* 11 (2015) 4640–4648. doi:10.1039/C5SM00411J.
URL <http://dx.doi.org/10.1039/C5SM00411J>
- [40] L. C. Johnson, B. J. Landrum, R. N. Zia, Yield of reversible colloidal gels during flow start-up: release from kinetic arrest, *Soft Matter* 14 (2018) 5048–5068. doi:10.1039/C8SM00109J.
URL <http://dx.doi.org/10.1039/C8SM00109J>

- [41] J. D. Park, K. H. Ahn, N. J. Wagner, Structure-rheology relationship for a homogeneous colloidal gel under shear startup, *J. Rheol.* 61 (1) (2016) 117–137. doi:10.1122/1.4971993.
URL <https://doi.org/10.1122/1.4971993>
- [42] M. Kim, J.-E. Bae, N. Kang, K. Soo Cho, Extraction of viscoelastic functions from creep data with ringing, *J. Rheol.* 59 (1) (2014) 237–252. doi:10.1122/1.4904394.
URL <https://doi.org/10.1122/1.4904394>
- [43] C. Cianci, D. Chelazzi, G. Poggi, F. Modi, R. Giorgi, M. Laurati, Hybrid fibroin-nanocellulose composites for the consolidation of aged silk, *Coll. Surf. A in press* (2021). doi:10.1016/j.colsurfa.2021.127944.
- [44] C. Macosko, R. Larson, K. (Firm), *Rheology: Principles, Measurements, and Applications*, Advances in interfacial engineering series, VCH, 1994.
URL <https://books.google.it/books?id=XXspAQAAAJ>
- [45] T. Sentjabrskaja, J. Hendricks, A. R. Jacob, G. Petekidis, S. U. Egelhaaf, M. Laurati, Binary colloidal glasses under transient stress- and strain-controlled shear, *J. Rheol.* 62 (1) (2018) 149–159. doi:10.1122/1.5009193.
URL <https://doi.org/10.1122/1.5009193>
- [46] M. Laurati, G. Petekidis, N. Koumakis, F. Cardinaux, A. B. Schofield, J. M. Brader, M. Fuchs, S. U. Egelhaaf, Structure, dynamics, and rheology of colloid-polymer mixtures: From liquids to gels, *J. Chem. Phys.* 130 (13) (2009) –. doi:http://dx.doi.org/10.1063/1.3103889.
- [47] A. Zaccone, H. Wu, E. Del Gado, Elasticity of arrested short-ranged attractive colloids: Homogeneous and heterogeneous glasses, *Phys. Rev. Lett.* 103 (2009) 208301. doi:10.1103/PhysRevLett.103.208301.
URL <https://link.aps.org/doi/10.1103/PhysRevLett.103.208301>
- [48] L. C. Johnson, R. N. Zia, E. Moghimi, G. Petekidis, Influence of structure on the linear response rheology of colloidal gels, *J. Rheol.* 63 (4) (2019) 583–608. arXiv:<https://doi.org/10.1122/1.5082796>, doi:10.1122/1.5082796.
URL <https://doi.org/10.1122/1.5082796>
- [49] R. Tanaka, Y. Kashiwagi, Y. Okada, T. Inoue, Viscoelastic Relaxation of Cellulose Nanocrystals in Fluids: Contributions of Microscopic Internal Motions to Flexibility, *Biomacromolecules* 21 (2) (2020) 408–417. doi:10.1021/acs.biomac.9b00943.
URL <https://doi.org/10.1021/acs.biomac.9b00943>
- [50] M. Dinkgreve, J. Paredes, M. M. Denn, D. Bonn, On different ways of measuring “the” yield stress, *J. Non-Newton. Fluid Mech.* 238 (2016) 233–241. doi:<https://doi.org/10.1016/j.jnnfm.2016.11.001>.
URL <https://www.sciencedirect.com/science/article/pii/S0377025716302774>

- 677 [51] R. R. Fernandes, D. E. V. Andrade, A. T. Franco, C. O. R. Negrão, The yielding
678 and the linear-to-nonlinear viscoelastic transition of an elastoviscoplastic mate-
679 rial, *J. Rheol.* 61 (5) (2017) 893–903. doi:10.1122/1.4991803.
680 URL <https://doi.org/10.1122/1.4991803>
- 681 [52] A. Le Grand, G. Petekidis, Effects of particle softness on the rheology and yield-
682 ing of colloidal glasses, *Rheol. Acta* 47 (5) (2008) 579–590. doi:10.1007/
683 s00397-007-0254-z.
684 URL <https://doi.org/10.1007/s00397-007-0254-z>
- 685 [53] G. J. Donley, P. K. Singh, A. Shetty, S. A. Rogers, Elucidating the g'' over-
686 shoot in soft materials with a yield transition via a time-resolved experimen-
687 tal strain decomposition, *Proc. Nat. Acad. Sci.* 117 (36) (2020) 21945–21952.
688 arXiv:<https://www.pnas.org/content/117/36/21945.full.pdf>, doi:
689 10.1073/pnas.2003869117.
690 URL <https://www.pnas.org/content/117/36/21945>
- 691 [54] W. Philippoff, Vibrational Measurements with Large Amplitudes, *Trans. Soc.*
692 *Rheol.* 10 (1) (1966) 317–334. doi:10.1122/1.549049.
693 URL <https://doi.org/10.1122/1.549049>
- 694 [55] K. Hyun, M. Wilhelm, C. O. Klein, K. S. Cho, J. G. Nam, K. H. Ahn, S. J.
695 Lee, R. H. Ewoldt, G. H. McKinley, A review of nonlinear oscillatory shear
696 tests: Analysis and application of large amplitude oscillatory shear (LAOS), *Prog.*
697 *Polym. Sci.* 36 (12) (2011) 1697 – 1753.
- 698 [56] D. V. Denisov, M. T. Dang, B. Struth, A. Zacccone, G. H. Wegdam, P. Schall,
699 Sharp symmetry-change marks the mechanical failure transition of glasses, *Sci.*
700 *Rep.* 5 (1) (2015) 14359. doi:10.1038/srep14359.
701 URL <https://doi.org/10.1038/srep14359>